High Strength Conductive Composites with Plasmonic Nanoparticles Aligned on Aramid Nanofibers

Jing Lyu[1,2,3], Xinzhi Wang[1,2,4], Lehao Liu[1,2,3], Yoonseob Kim[1,2], Ekembu K. Tanyi[5], Hang Chi[6], Wenchun Feng[1,2], Lizhi Xu[1,2], Tiehu Li[3], Mikhail A. Noginov[5], Ctirad Uher[6], Mark D. Hammig[7], Nicholas A. Kotov[1,2,8,9,10] *

[1] Department of Chemical Engineering, University of Michigan, Ann Arbor, MI 48109, USA;

[2] Biointerfaces Institute, University of Michigan, Ann Arbor, MI 48109, USA;

[3] School of Materials Science and Engineering, Northwestern Polytechnical University, Xi'an 710072, P. R. China;

[4] School of Energy Science and Engineering, Harbin Institute of Technology, Harbin 150001, P. R. China;

[5] Center for Materials Research, Norfolk State University, Norfolk, VA 23504, USA;

[6] Department of Physics, University of Michigan, Ann Arbor, MI 48109, USA;

[7] Department of Nuclear Engineering and Radiological Sciences, University of Michigan, Ann Arbor, MI 48109, USA;

[8] Department of Materials Science and Engineering, University of Michigan, Ann Arbor, MI 48109, USA;

[9] Department of Biomedical Engineering, University of Michigan, Ann Arbor, MI 48109, USA;

[10] Michigan Center for Integrative Research in Critical Care, 2800 Plymouth Road, Ann Arbor, MI 48109, USA.

ABSTRACT: Rapidly evolving fields of biomedical, energy, and (opto)electronic devices bring forward the need for deformable conductors with constantly rising benchmarks for mechanical properties and electronic conductivity. The search for conductors with improved strength and strain inspired the multiple studies of nanocomposites and amorphous metals.

This is the author manuscript accepted for publication and has undergone full peer review but has not been through the copyediting, typesetting, pagination and proofreading process, which may lead to differences between this version and the Version of Record. Please cite this article as doi: 10.1002/adfm.201603230.

This article is protected by copyright. All rights reserved.

Author Manuscript

However, finding conductors that defy the boundaries of classical materials, and exhibit simultaneously high strength, toughness, and fast charge transport while enabling their scalable production, remains a difficult materials engineering challenge. Here we describe composites made from aramid nanofibers (ANFs) and metallic nanoparticles (NPs) that offer a new toolset for engineering high strength high strain flexible conductors. ANFs are derived from Kevlar™ macrofibers and retain the high mechanical properties and temperature resilience characteristic of the parent material. Gold nanoparticles (Au NPs) are infiltrated into a porous, free-standing aramid matrix, becoming aligned on ANFs, which reduces charge percolation threshold and facilitates charge transport. Taking advantage of high temperature resilience of ANFs, thermal annealing at 300 °C results in the Au-ANF composites with electrical conductivity of 1.25×10^4 S·cm^{-1}, combined with a tensile strength of 96 MPa, a Young's modulus of 5.29 GPa, and a toughness of 1.3 MJ/m^3. These parameters exceed those of most of the composite materials known, and are comparable to those of amorphous metals but have no volume limitations. Simplicity and scalability of their production should be noted. Moreover, NP-ANF composites are made from human-friendly components often desirable for biomedical and electronic devices. The plasmonic optical frequencies characteristic for constituent NPs are present in the composites with ANFs enabling plasmon-based optoelectronic applications.

KEYWORDS: high strength composites, flexible conductors, amorphous metals, nanocomposites, gold nanoparticles, plasmonic composites, aramid nanofibers, electrical conductivity, Kevlar™.

TOC:

Author Manuscript

This article is protected by copyright. All rights reserved.

Author Manuscript

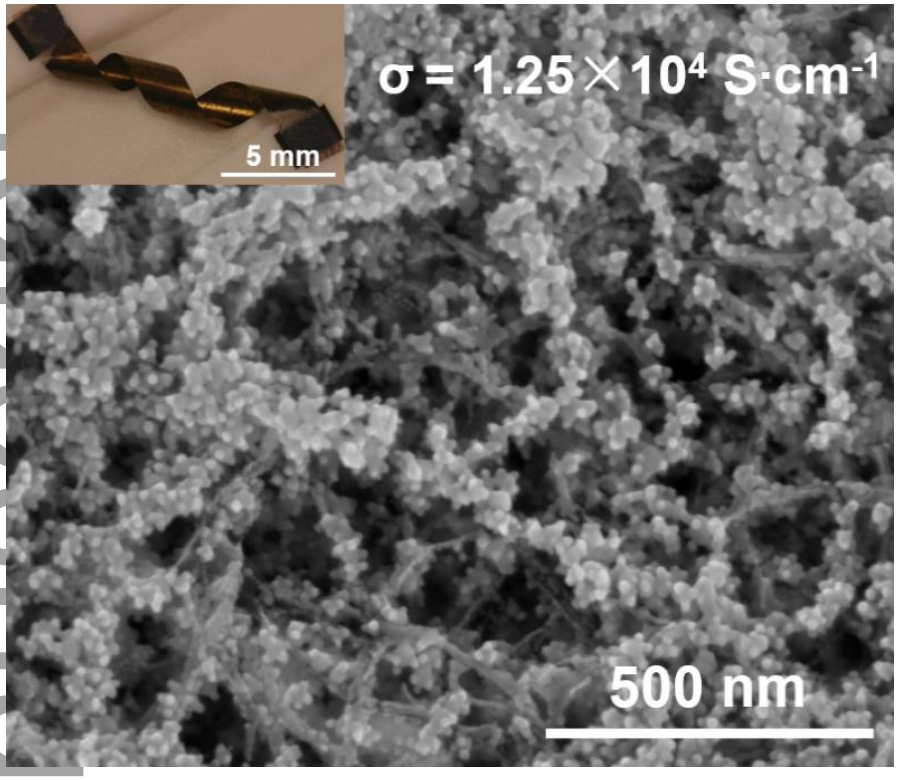

This article is protected by copyright. All rights reserved.

INTRODUCTION

Emerging energy,[1–5] transportation,[6,7] military,[7,8] biomedical,[9] electronic[5,10–12] and other technologies[13,14] create constantly increasing demand for materials with high mechanical strain/stress, electrical conductivity, thermal stability, toxicology, novel optical,[15] and other properties.[6,16,17] In the last decade these needs inspired extensive research on amorphous metals - unique conductors prepared by rapid vitrification of molten alloys of Au, Pd, or Pt.[18–21] Such alloys represent a special class of materials that combine high mechanical and reasonable electrical properties (**Table 1**).[22–24] The absence of crystallites, grain boundaries, and dislocations in the amorphous structure results in high strength, elastic strain limit, corrosion resistance, and in some cases, substantial ductility.[18,25–28] Although these materials can be used in nanoscale molding[18] and some other applications that do not require large volumes, these materials are difficult utilize due to rapid recrystallization processes transforming glasses into (meso)crystalline material. The strength of amorphous metals decrease rapidly at higher temperatures. The physical dimensions of conducting elements from amorphous metals are also limited to small flakes or disk-shaped foils[29] and their temperature sensitivity creates problems with processing, particularly for complex shapes.[30]

Alloy	Electrical Conductivity	Stress	Strain (%)	Young's Modulus	Reference

This article is protected by copyright. All rights reserved.

Author Manuscript

	($S \cdot cm^{-1}$)	(GPa)		(GPa)	
$Pd_{40}Cu_{30}Ni_{10}P_{20}$	1.85×10^4	1.72	1.87	92	[26, 27]
$Pd_{81}Cu_5Si_{14}$	1.56×10^4	1.2	2.00	60.1	[33]
$Au_{55}Cu_{25}Si_{20}$	-	1.0	1.43	69.8	[31]
$Au_{49.5}Ag_{5.5}Pd_{2.3}Cu_{26.9}Si_{16.3}$	-	1.2	1.61	74.4	[31]
$Zr_{41.2}Ti_{13.8}Cu_{12.5}Ni_{10}Be_{22.5}$	2.28×10^4	1.86	1.96	0.95	[23, 32]

Table 1. Electrical conductivity and mechanical properties of typical amorphous metallic alloys.

Hybrid organic-inorganic nanocomposites represent another more common venue to address the challenge of high strength conductors. High mechanical properties and fast charge transport is common for many nanoscale conductors. Although the transfer of these properties from nanoscale to macroscale has fundamental threshholds,[34,35] promising nanocomposite conductors have been made in the form of nanocomposite films, free-standing sheets, and fabrics.[36,37] They show promise as wearable electronic devices,[38–40] biosensors,[40–42] high performance batteries,[4,43–47] and neural implants.[39,48–50] While these composites are mostly based on carbon nanostructures, a lot of them were made from metal nanoparticles (NPs).[51–55] However, the metal NP content in these composites is usually low[56] except several cases of materials specifically design for high inorganic volume fraction.[57,58] Nanocomposites from metal nanostructures are attractive materials for materials design of high strength conductors due to additional plasmonic optical effects and

This article is protected by copyright. All rights reserved.

Author Manuscript

self-assembly phenomena[59] that are useful in for optoelectronics. Vacuum-assisted filtration (VAF) and layer-by-layer (LBL) assembly[60] lead to composites with high loading of Au NPs that helps realizing high electrical conductivity attributed to self-organization processes taking place with NPs imbedded in the flexible polymer matrix.[61] Kirigami patterning offers new tools to resolve the materials property conflict between high strain and high conductivity.[62]

In this study, we are seeking new approaches to produce materials with high strength and high conductivity taking advantage of both nanoscale materials that became available only recently and NP self-organization. Here we describe the possibility to prepare free standing flexible composite material with these parameters made from prototypical metal NPs and aramid nanofibers (ANFs).[63] The latter represent a versatile new building block among nanomaterials[64–67] and were chosen because ANFs inherits from the parent Kevlar™ nanofibers high chemical/thermal stability and exceptional mechanical performance (stiffness: 109 GPa and strength: 3.6 GPa), High nanoscale porosity of ANF matrixes[14,68] and the abundance of surface amide groups on ANFs enables further functionalization of the nanofibers and incorporation of other components onto and between aramid chains.[8] Also important prioduction of ANFs is easy to scale.

Au-ANF films made by spin-coating were infiltrated with Au NPs by VAF. Although this method does not provide as high degree of structural engineering control of nanocomposites as one can obtain in LBL,[69,70] it is simpler than previously reported fabrication techniques for NP composites.[71] Compared with other high strength high

This article is protected by copyright. All rights reserved.

Author Manuscript

conductance materials, for instance amorphous metals, this synthetic method not have severe temperature or volume restrictions. The open porous[72] structure of ANF films reminiscent of cellular forms of graphene[73–76] allows high loading of Au NPs to form an interconnected three-dimensional conductive network that increases their conductivity. The nanoscale fibers present a convenient template onto which NPs can effectively self-assemble[14,77] to produce particle chains that facilitate charge transport. In a perspective of fundamental materials science, the nanoscale porosity and fibrous morphology of the ANF matrix opens the door for mesoscale architectonics[78] – the materials engineering approach with particularly suitability in this case. Viewing these ANF-NP composites in this perspective makes also possible extension of this work to multiplicity of other nanoscale composites and related optoelectronic properties. After thermal annealing at 300 °C, Au-ANF film demonstrates electric conduction of 1.25×10^4 S·cm^{-1}, tensile strength of 96 MPa, Young's modulus of 5.29 GPa, and toughness of 1.3 MJ·m^{-3}, properties that are comparable or surpass those of most nanocomposites and many metals. These properties make Au-ANF film suitable for many applications.

RESULTS AND DISCUSSION

***Preparation of Au-ANF Composites*.** An ANF solution was synthesized according to the previously reported method.[63] It started from the preparation of the viscous dark red solution obtained by adding bulk Kevlar threads into dimethyl sulfoxide (DMSO) in the presence of potassium hydroxide (KOH) followed by stirring for three weeks (**Supporting Information, Figure S1**). Weakening of hydrogen bonds combined with strengthening of

This article is protected by copyright. All rights reserved.

Author Manuscript

electrostatic repulsion between the polymer chains, the bulk aramid macroscale fibers can be chemically transformed into nanofibers. Importantly, the hydrophobic attraction and π-π stacking in the polymer backbone limited the extent of this destruction down to the level of individual polymer chains.[63] The diameter of the resulting nanofibers is determined by the equilibrium of total energy of repulsive and attractive forces which makes them similar to supraparticles.[79–81] Transmission electron microscope (TEM) images showed that the average diameter of ANFs after dissolution was about 20 nm and their lengths were in the range of several micrometers (**Supporting Information Figure S1a**).

Spin coating was employed for the preparation of the ANF films from this solution. This process is very versatile in controlling the thicknesses of the films via tuning the rotation speed and time. The ANF hydrogel is formed by immersing the films on the glass substrates into deionized water (DI water) to remove the DMSO and protonate ANFs. Fortuitously, the hydrogel spontaneously separated from the substrate during this process. In order to preserve the nanoscale morphology of ANF hydrogels during drying, supercritical CO_2 drying was applied. This is required as the sponge-like structure of the ANF hydrogel can collapse during an ordinary drying process due to the surface tension in the liquid body that pulls against any solid structure with which the liquid might be in contact. The semitransparent, flexible, and porous ANF films formed after supercritical drying are shown in **Figure 1a** (left). Scanning electron microscopy (SEM) images of the microscale morphology of ANF films are shown in **Figures 1b-d**. A side view cross-sectional image (**Figure 1b**) shows the sponge-like

Author Manuscript

This article is protected by copyright. All rights reserved.

structure of porous ANF films confirming the open pore structure of the ANF films (**Figures 1c, d**).

To investigate the thermal stability of ANFs, thermogravimetric analysis (TGA) of Kevlar threads and ANF films were performed at a heating rate of 10 °C/min under nitrogen atmosphere (**Supporting Information Figure S1b**). The TGA curves indicate that the ANF films showed extraordinary thermal stability, similar to the bulk Kevlar threads. This is exciting because thermal stability is necessary to address the bottleneck preventing widespread application of flexible conductors composed of polymer substrates.

Au NPs were synthesized by a citrate-stabilized method because the citrate coating was expected to present a minimal barrier for charge transfer between Au NPs. In addition, the citrate-stabilized Au NPs, about 13 nm in diameter, are well dispersed in aqueous solution, as reported by our group previously (**Supporting Information Figure S2. a, b**).[61]

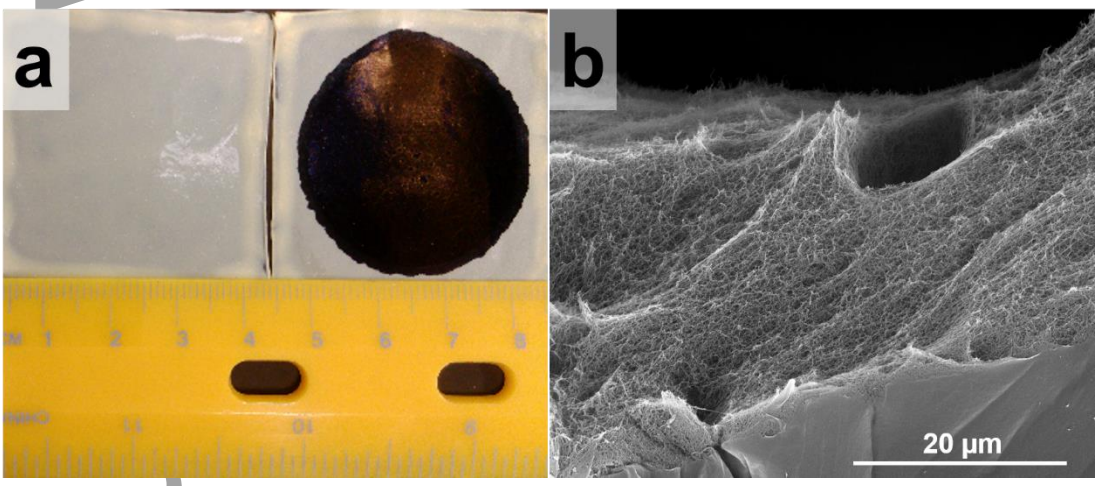

Author Manuscript

This article is protected by copyright. All rights reserved.

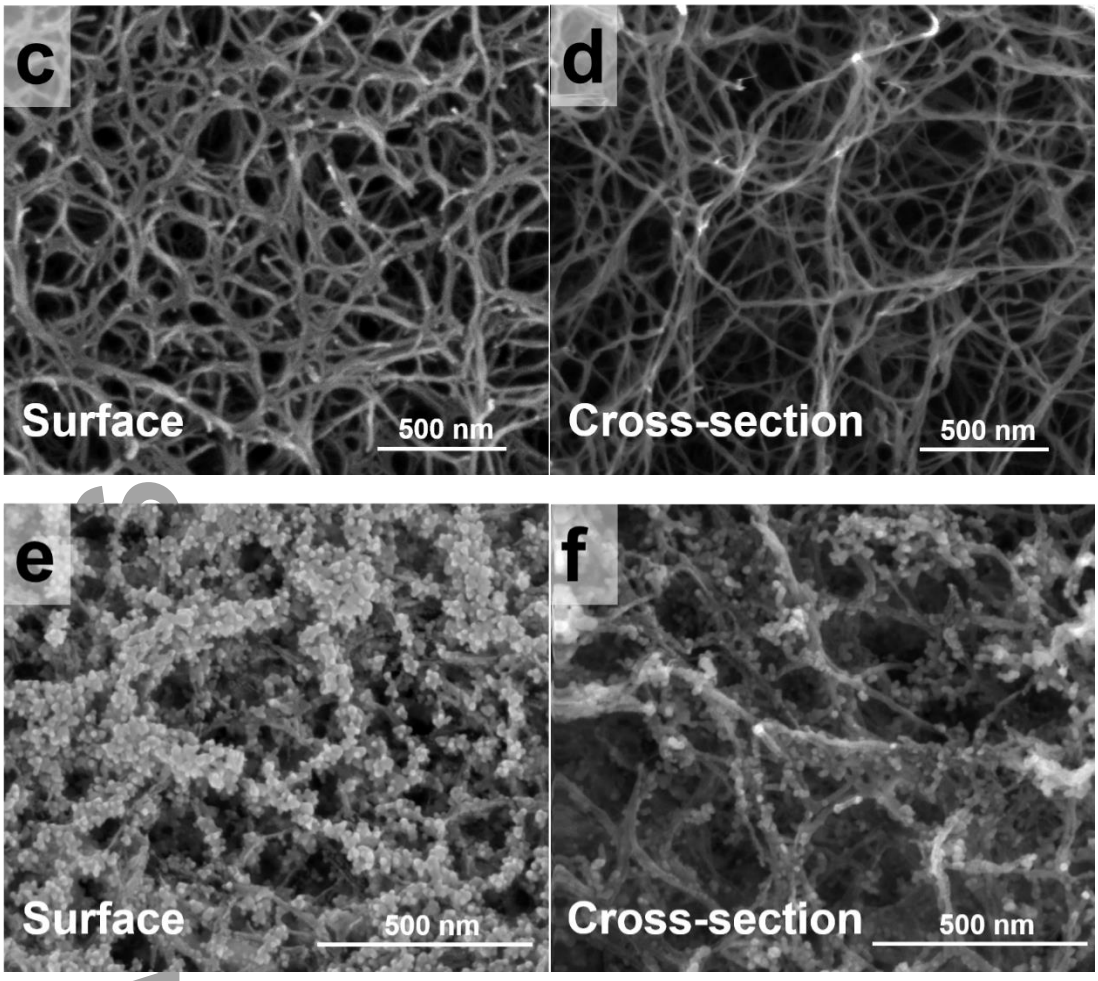

Figure 1. a, Photograph of ANF film and Au-ANF film made using supercritical CO_2 dying. b, Off-angle cross-section SEM image of ANF film. c, d, SEM images of ANF film. e, f, SEM images of Au-ANF film.

At the onset of the study, we incorporated plasmonic Au NPs into ANF films by adsorbing them from a concentrated Au NPs dispersion. Au NPs diffused into the porous films spontaneously and resulted in a measurable volume uptake after a week. From SEM images we could see that Au NPs decorated the surface of ANFs uniformly (**Supporting Information Figure S3**). However, this diffusion reached saturation at low volume uptake,

This article is protected by copyright. All rights reserved.

which did not enable the films to acquire the desired conductivity. An alternative method, vacuum filtration, was employed to incorporate Au NPs into the ANF films. During this process, ANF films served as the filter membranes into which Au NPs were trapped (**Supporting Information Figure S4a**).

Au-ANF films reveal an unambiguous metallic appearance (**Figure 1a**, right). In order to demonstrate that Au NPs had been trapped within the ANF films, they were subjected to SEM and X-ray diffraction (XRD) analysis. The Au NPs adsorbed along the ANFs throughout the ANF matrix, and an interconnected Au NPs network structure formed (**Figure 1e, f**). This interconnected network may establish electrical conduction pathways throughout the whole composite if the Au NP volume fraction is sufficiently high throughout the bulk. The XRD patterns of the ANF films and Au-ANF films are shown in **Supporting Information Figure S5a.** The diffraction peaks at 38.1°, 44.2°, 64.5°, and 77.7° were attributed to (111), (200), (220), and (311) planes of a face-centered-cubic (fcc) Au (JCPDS 04-0784).[82] As expected, the XRD peaks indicated that the Au NPs kept the original crystalline domains after being incorporated into the films.

The pore sizes of ANF films are about 200-600 nm, much larger than the diameters of the Au NPs. Initially, all the Au NPs were trapped in the films and then gradually a few Au NPs passed through the films during vacuum filtration. The adsorption mechanism for citrate covered Au NPs on the ANFs could be explained by hydrogen bonding. The ANF backbones have multitudinous amide groups, each containing a hydrogen atom acting as a hydrogen bound acceptor, while the Au NPs stabilized by citrate are capped by carboxylic

Author Manuscript

This article is protected by copyright. All rights reserved.

acid groups. Upon contact, hydrogen bonding occurs, which binds the Au NPs very tightly to the ANFs (**Supporting Information Figure S4b**). FT-IR spectroscopy was carried out to verify this interaction between ANFs and Au NPs. The infrared absorption peaks characteristic of ANFs were observed at 3326 cm^{-1} (N-H stretching vibrations), 1650 cm^{-1} (C=O stretching vibrations), 1545 cm^{-1} (N-H deformation), and 1516 cm^{-1} (C=C stretching vibrations).[63] After incorporation of Au NPs, a broad peak around 3300 cm^{-1} (O-H stretching vibrations) was observed, indicative of the formation of hydrogen bonds (N-H···O). In addition, the IR band of C=O bonds shifts to lower frequency (1640 cm^{-1}) because of the hydrogen bonds formed by C=O groups with N-H groups (**Supporting Information Figure S5b**).[83]

Spectroscopic studies. The reflectance and absorbance spectra of ANF films and Au-ANF films with different Au concentrations (15.7 vol. %, 3.4 vol. %, and 1.0 vol. %) were measured. The characteristic onset of bulk Au reflectance (**Supporting Information Figure S6a**) was observed in all three Au-ANF films–more pronounced at high concentration of Au NPs, and still seen in samples with low Au concentration (**Supporting Information Figure S7**). At high Au concentration, the film's transmission was nearly equal to zero, as expected of thick bulk metallic films. At the same time, the absorbance band characteristic of plasmon resonance in individual Au NPs (**Supporting Information Figure S6b**) was observed at lower Au concentrations (**Figure 2a**). None of the signature metallic responses depicted in Au-ANF films was shared by the pure ANF films (**Figure 2b**). (Sharp edge of absorbance at ≈0.42 μm is related to the onset of the strong absorption band at ≤ 0.4 μm).

Author Manuscript

This article is protected by copyright. All rights reserved.

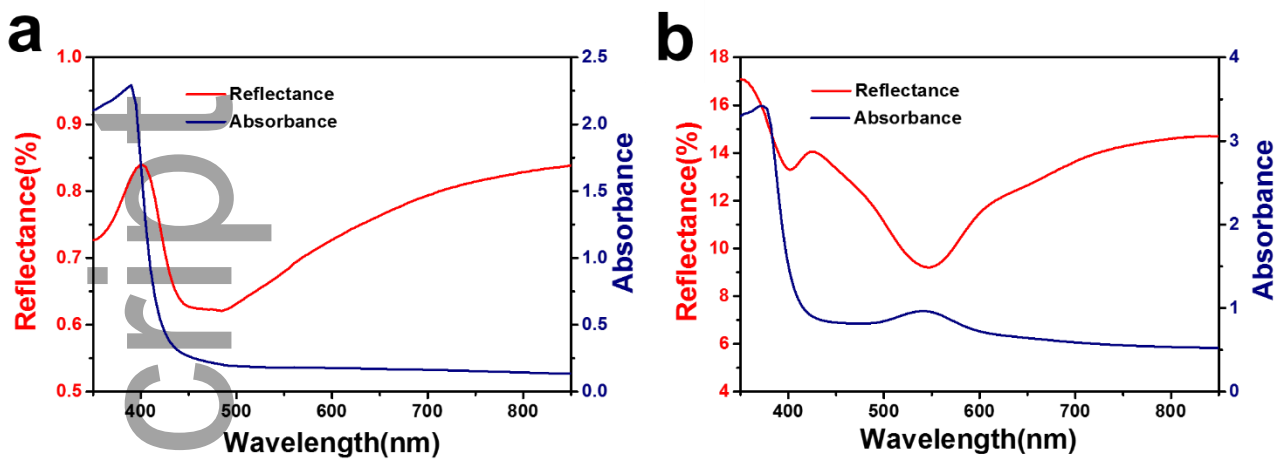

Figure 2. Reflectance (red) and absorbance (blue) spectra of (a) ANF film and (b) Au-ANF film with 1.0 vol. % Au NPs.

The fact that in the Au-ANF films with low concentrations of Au NPs (**Figure 2a and Supporting Information Figure S7b**), the reflectance spectra were characteristic of bulk gold and the absorbance spectra were characteristic of individual Au NPs with typical plasmon band at ca. 545 nm was surprising. However, it can be understood taking into account that (1) The reflectance measurements probe the sample's surface, which has a higher concentration of Au NPs, while the transmittance measurements probe the volume, where the concentration of Au NPs is lower; and (2) transmitted and reflected photons experience different numbers of scattering events. Therefore, the transmittance and reflectance measurements probe the same ANF films in different ways, which may explain the seemingly paradoxical coexistence of metallic bulk and plasmonic NP properties.

Author Manuscript

This article is protected by copyright. All rights reserved.

Electrical properties of Au-ANF films. The pure ANF films are insulators but the introduction of Au NPs generates electrical conductivity in the Au-ANF composite films. This transition from insulator to conductor is attributed to the loaded Au NPs and the formation of conductive pathways within the composite when the average distance between Au NPs became sufficiently small, affording efficient tunneling or direct electron transport. Similarly to the previous studies of composite materials with some degree of axial organization of NPs into bands and chains show much improved electrical transport[14,51,55,61,84,85] as well as interesting optical properties originating from plasmonic effects.[52,53,86,87]

To further demonstrate the electrical properties of these Au-ANF films, we measured the electrical conductivity as a function of Au volume fraction from 13.9 vol% to 34.7 vol%. The volume fraction of Au NPs can be simply controlled by adjusting the volume of the Au NP solution during the vacuum filtration procedure (**Supporting Information Figure S8a**). The electrical conductivity increases with Au NPs loading into the ANF matrices (**Figure 3a**). At an Au content of 13.9 vol% and 14.7 vol%, the composite films did not show any pronounced electrical conductivity. With an increased Au content to 15.7 vol% and 19.6 vol%, a sharp rise in the conductivity was observed. At 15.7 vol%, and 19.6 vol%, the conductivities were 9.64×10^{-4} S·cm^{-1} and 25.36 S·cm^{-1}, respectively. Further increased Au loading to 24.8 vol% and 28.9 vol% led to raised conductivities to 114.33 S·cm^{-1} and 204.31 S·cm^{-1}, respectively. At an Au concentration of 34.7 vol%, the conductivity reached a value of 1.03×10^{3} S·cm^{-1}. This trend electrical conductivity with respect to Au NPs loading can be explained using percolation theory, which describes the transition from a state of spatially

This article is protected by copyright. All rights reserved.

Author Manuscript

restricted connections of conductive elements to a state of infinite network connections. When the conductive filler volume fraction is low, the average distance between metal particles was so large that conduction was restricted. But when the conductive filler reached a critical concentration, a physical path was formed, through which the current could flow by percolating the entire system. In the vicinity of the transition, the electrical conductivity of the composite increases by orders of magnitude which is expressed via a power-law relationship used in classical percolation theory

$$\sigma = \sigma_0 (V_f - V_0)^t$$

where σ_0 is the conductivity of the filler, V_o is the critical concentration or percolation threshold, V_f is the volume fraction of the filler and t is the critical exponent.[88] Importantly, the experimentally determined value for the percolation threshold of the Au NP-ANF system is 15.7 vol% (**Figure 3a**), which can be compared to 18.3 % for a randomly packed network of spheres.[89] The reduction of the percolation threshold can be attributed to the alignment of NPs on the constituent nanofibers.

The investigation of the mechanisms of conduction in Au-ANF films is both academically and practically significant. The conductivity linearly declines with increasing temperature from 5 to 300 K indicating metallic conduction behavior (**Figure 3c**) shows the temperature dependence of the conductivity for supercritical dried Au-ANF films. Fitting the temperature dependence of conductivity with variable-range hopping and tunneling

Author Manuscript

This article is protected by copyright. All rights reserved.

conduction mechanism equations revealed that the electron transfer mechanism was not dominated in this manner (**Supporting Information Figure S9**).

Mechanical properties of Au-ANF films. The mechanical properties of Au-ANF films are critical for the design of devices. We found that the Au-NPs composites combine high electrical conductivity and high strength with the latter considerably exceeding other composites as seen from Table 2. However, the tensile strength gradually decreases with the increase in the Au NPs volumetric fraction (**Figure 3d**). The maximum tensile strength decreased from 196 MPa (pure ANF films) to 96 MPa (34.7 vol% Au NPs). However, the Young's modulus increased from 1.7 GPa to 3.2 GPa with an increase Au NPs concentration (**Figure 3e**). The optimization between the electrical conductivity and tensile properties of the nanocomposite can be realized by properly controlling the Au NPs volumetric fraction.

The maximum tensile strength of Au-ANF composite films depend on the weakest fracture path throughout the films. Au NPs are likely to affect the tensile strength via two opposing mechanisms. One is a weakening effect due to the NP-induced stress concentration, and the second is a reinforcing effect since they may serve as barriers to crack growth. In this case, the weakening effect is predominant, thus the Au-ANF films strength are lower than that of the pure ANF films.[90] The strain at break decreased with the increase in Au NP volumetric fraction as well. This is due to the interactions between Au NPs and the ANF matrix, which restricts the movement of polymer chains. This behavior is typical of polymer composites reinforced with fillers of nanoscale dimension.[91] Generally,

Author Manuscript

This article is protected by copyright. All rights reserved.

the addition of higher amounts of filler content to polymers leads to poor processability and inferior mechanical performance.[92]

Flexibility is significant for high-strength conductor to be employed in wearable electronics[93] and other applications. A film with Au content of 24.8 vol% was subjected to tension bending (**Figure 3b** inset). The Au-ANF film exhibited excellent mechanical flexibility; there was no significant change in electrical conductivity even after 1,000 bending cycles, and the tensile stress and Young's modulus remained unchanged within experimental error (**Figures 3f and 3g**).

Author Manuscript

This article is protected by copyright. All rights reserved.

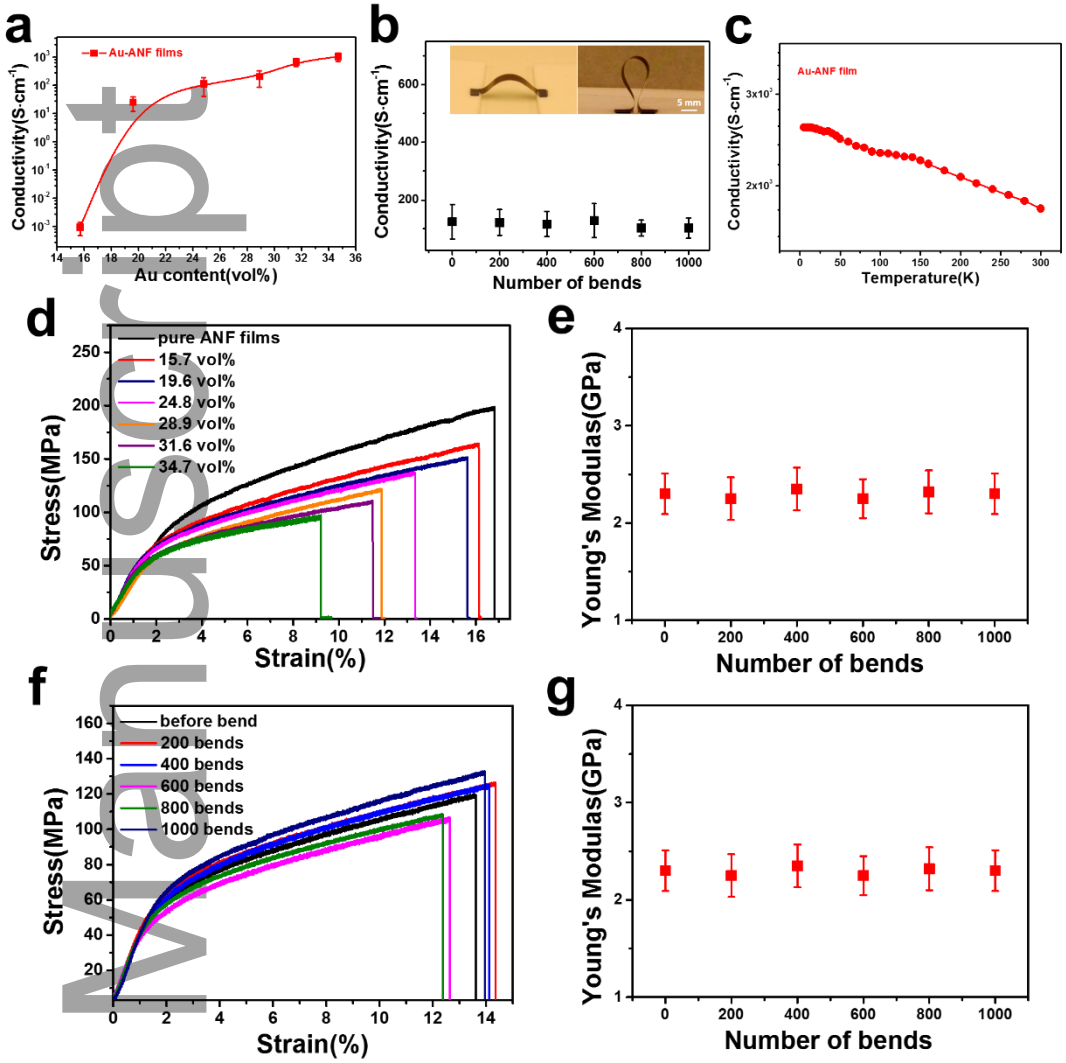

Figure 3. a, The conductivity of Au-ANF films as a function of Au NPs volumetric fraction. b, The conductivity versus number of bends for Au-ANF film with 24.8 vol% Au fraction. c, Temperature dependence of conductivity for Au-ANF films. d, e, The tensile stress and Young's modulus of Au-ANF films with different Au NP volumetric fractions. f, g, The tensile stress and Young's modulus of Au-ANF film (24.8 vol. % Au) as a function of number of bends.

Thermal Annealing. Exploiting the high temperature stability of ANFs, the conductivity of Au-ANF films can be improved by thermal annealing. This enhances the crystallinity of,

This article is protected by copyright. All rights reserved.

Author Manuscript

and connectivity between, metal NPs[94] at temperatures unsuitable for other polymers. Based on TGA results of ANF films and Au-ANF films (**Supporting Information Figure S1b and Figure S8**), we believe that ANFs will remain stable at temperatures as high as 400 °C. The coalescence of Au NPs can be achieved at temperatures of ~10% of the melting points of their bulk counterparts (1336 K), due to their high surface area to volume ratio and surface atom instability.[95] In addition, at above 175 °C, the citrate stabilizer decomposed into H_2O and CO_2, which migrated away from the inter-particle regions and improved contact between the Au NPs.[96] Considering these observations, thermal annealing temperatures between 200 °C and 400 °C were employed.

The conductivity of Au-ANF films with 34.7 vol% Au content improved with increasing annealing temperature, rising from 1.03×10^3 S·cm^{-1} to 1.25×10^4 S·cm^{-1} after annealing for 20 min at 300 °C. Increasing the annealing temperature to 400 °C, the conductivity reached 6.3×10^4 S·cm^{-1} (**Figure 4a).**

The increased intensities of the XRD peaks provided evidence that thermal annealing improved the Au NPs crystallinity. **Figure 4b** shows the XRD patterns of the as-prepared Au-ANF film with 34.7 vol% Au content and the films obtained by annealing under temperatures ranging from 200 °C to 400 °C. All of the films exhibited the indexed diffraction peak consistent with the standard values of a face-centered-cubic (fcc) Au structure (JCPDS 04-0784). As annealing temperatures increased from 200 °C to 400 °C, the Au(111), Au(200), Au(220), and Au(311) peaks increased their amplitude and decreased their full width at half maximum (FWHM) as a result of a gradual improvement in

Author Manuscript

This article is protected by copyright. All rights reserved.

crystallinity and reduced crystal defects.[94] The average crystallite size of Au NPs calculated from the Scherrer equation increased from 14.8 nm to 20.5 nm after annealing (**Supporting Information Table S1**), which was in agreement with the SEM images (**Figures 4e-j**).

While thermal annealing increases conductivity, that improvement came at the expense of a decrease in ultimate strain[95], which dropped from 9.2 % to 1.0%. The tensile strength of the Au-ANF films was maintained at about 95 MPs at temperatures under 300 °C (**Figure 4c**), while the Young's modulus increased from 3.07 GPa to 5.29 GPa (**Figure 4d**). When the annealing temperature exceeded 300 °C, the tensile strength and Young's modulus tended to decrease. **Figures 4e-j** show SEM images of the Au-ANF films at different annealing temperatures. The microscopy images of the films indicated stronger inter-particle coalescence with increased annealing temperatures. When annealed at 200 °C, some of the Au NPs fused into larger NPs (**Figure 4f**). As the temperature increased to 300 °C, most of the Au NPs coalesced and formed irregularly shaped particles (**Figure 4h**). Increasing the annealing temperature to 400 °C, the irregularly shaped particles fused together to form a network throughout the entire Au-ANF films (**Figure 4j**).[70]

Author Manuscript

This article is protected by copyright. All rights reserved.

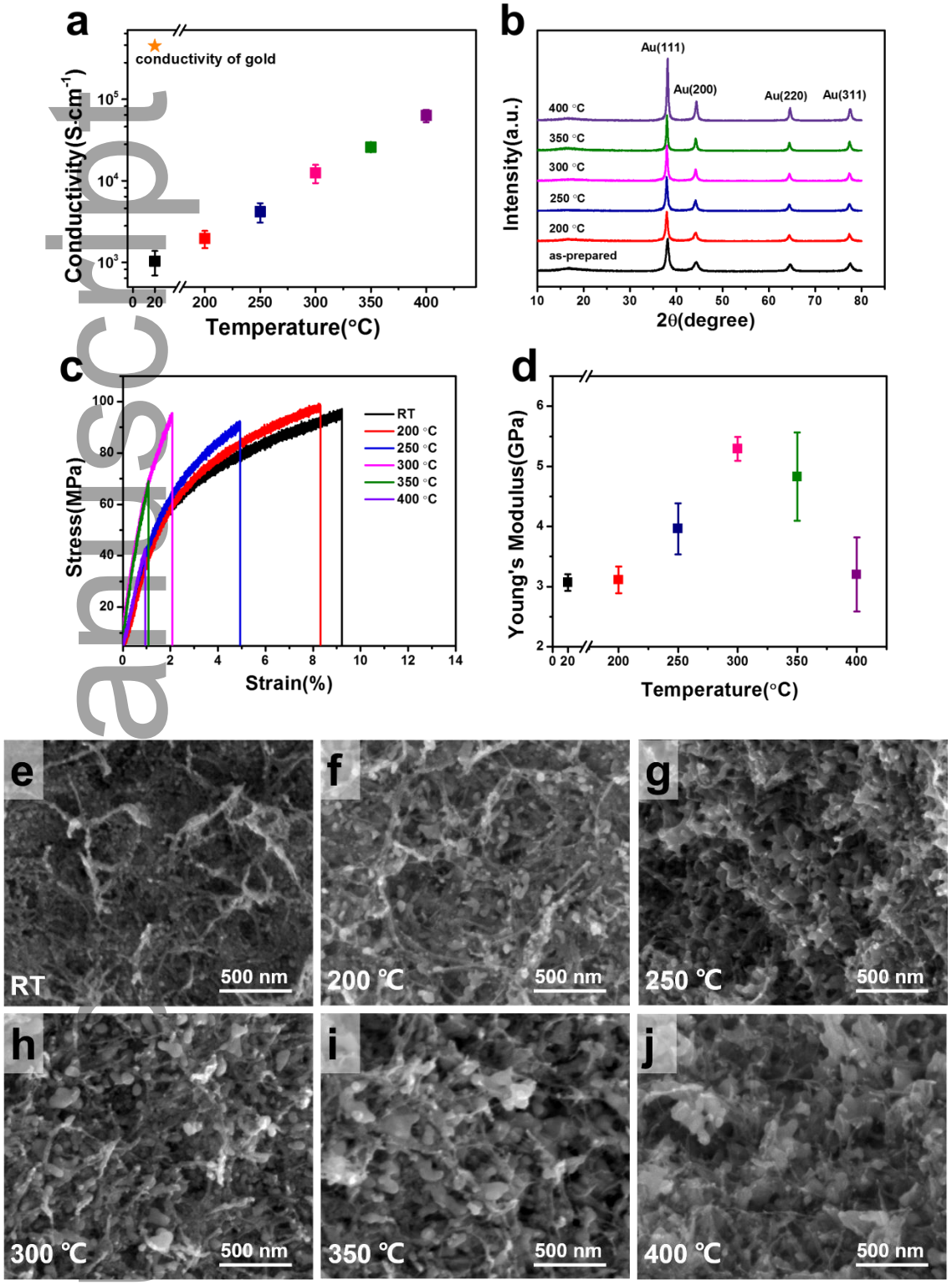

Figure 4. a, Electrical conductivity of supercritical dried Au-ANF films as a function of annealing temperatures (black - 20 °C, red - 200 °C, blue-250 °C, pink - 300 °C, green - 350 °C, purple - 400 °C). b, XRD patterns of the as-prepared Au-ANF films and the annealed Au-ANF films at various temperatures. c, The stress-strain curves

This article is protected by copyright. All rights reserved.

of supercritical dried Au-ANF films with different annealing temperatures. d, Young's modulus of supercritical dried Au-ANF films with different annealing temperatures. e-j, SEM images of supercritical dried Au-ANF films at different annealing temperatures.

The electrical conductivity and ultimate tensile strength of Au-ANF films are compared with those for nanocomposites (graphene based, CNT based, et al.) and amorphous metals (Ce-based, Pd-based, et al.) in **Figure 5**. The comparison shows that some graphene based nanocomposites, such as graphene/ANF and graphene/cellulose (data points 5 and 6) display electrical conductivity and ultimate strength higher than these of nanocomposites. Eectrical conductivity for composites is still 3-4 orders lower than that of Au-ANF films except LBL_assembled Au NPs/PU composite that exhibits high electrical conductivity, but lower ultimate strength to Au-ANF films. The amorphous metals display, however, higher ultimate strength with comparable electrical conductivity, however, the limited process-zone size restricts the structural use of amorphous metals to small components.

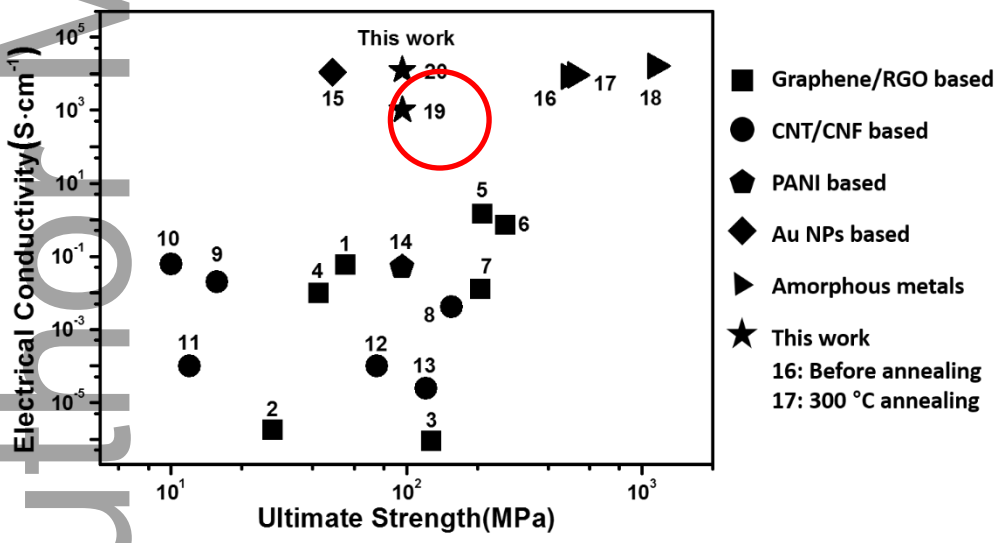

Figure 5. Comparison of electrical conductivity and ultimate strength of Au-ANF composite films with selected conductive nanocomposites (graphene based, carbon nanotube based, et al.) and amorphous metals.[61,66,97–112] (1: graphene/PVC (ref 97); 2: graphene/polypropylene (ref 98); 3: graphene/polyimide (ref 99); 4: RGO/PVDF

This article is protected by copyright. All rights reserved.

Author Manuscript

(ref 100); 5: graphene/ANF (ref 66); 6: graphene/cellulose (ref 101); 7: RGO/chitosan (ref 102); 8: CNT/PPE (ref 103); 9: CNT/polyethylene (ref 104); 10: MWNT/epoxy (ref 105); 11: MWNT/polyethylene(ref 106); 12: CNF/epoxy (ref 107); 13: MWNT/polyimide (ref 108); 14: PANI/bacterial cellulose (ref 109); 15: Au NPs/polyurethane (ref 61); 16: $Ce_{70}Al_{10}Cu_{20}$ or $Ce_{68}Al_{10}Cu_{20}Nb_2$ amorphous alloys (ref 110); 17: Al-Ln amorphous alloys (ref 111); 18: $Pd_{76}Cu_7Si_{17}$ thin film metallic glasses (ref 112); 19: Au-ANF film with 34.7 vol% Au content; 20: Au-ANF film after 300 °C thermal annealing.)

The observed conductivity of Au NP-ANF composites is most likely lower than the maximum performance possible. Conductivity can be improved by maximizing the uniformity of the conductance throughout the film depth. Although Au NPs are incorporated throughout the cross-section of the Au-ANF films (**Supporting Information Figure S10**), the electrical characterization of the films indicated that the volume fraction of Au NPs in the bulk is below the critical volume fraction necessary to percolate metallic-conduction through the entire film thickness. The alignment of NPs along ANF fibers makes charge transport possible, but can still be optimized further. **Figures 6a** and **b** show the current-voltage (IV) characteristics for the 24.8 vol% annealed film when probed either along the top surface (**Figure 6a**) or across the bulk (**Figure 6b**). Probing the top surface exhibits metallic conduction with lower resistivity as the annealing temperature was increased, while the bulk resistivity remained high regardless of the temperature conditioning, indicating that the bulk current leakage is roughly 10 orders of magnitude smaller than the surface current.

The formation of a conducting composite upon the insulating ANF network is also demonstrated in the capacitance-voltage (CV) curves of **Figure 6c**. The measured capacitances, in the range of 4 pF, from the ~2 × 2 mm^2 areal contact were consistent with that expected from a parallel plate capacitor bounding a mixed air ($C_{pure\ air}$ = 4.7 pF) and

This article is protected by copyright. All rights reserved.

Author Manuscript

Kevlar ($C_{bulk\ Kevlar}$ = 18.8 pF) dielectric. Possessing a means of control over the penetration depth of the conductive layer opens up the possibility of using the Au-ANF structure in a metal-insulator configuration, for use in high voltage capacitors or metal-insulator-metal sensors, as we could apply over 800 V to the film without breakdown-induced damage.

CONCLUSIONS: Au NPs were incorporated into a porous ANF matrix to realize materials with high strength and high electrical conductivity. This combination of properties is typically difficult to attain. Its feasibility in ANF-NP composites is associated with the high-strength ANF network serving as a backbone for assembly and the alignment of Au NPs. Their properties are comparable to amorphous metals while avoiding difficulties with processing, scalability, and brittleness. The Au-ANF composite films also demonstrate flexibility, creating a viable alternative to other flexible conductors based on nanoscale carbons (CNTs and graphene) or metallic nanowires. Future studies involving the design and engineering of high-performance polymeric composites may include the use of other plasmonics and metals in nanoscale form such as copper and silver NPs.

Author Manuscript

This article is protected by copyright. All rights reserved.

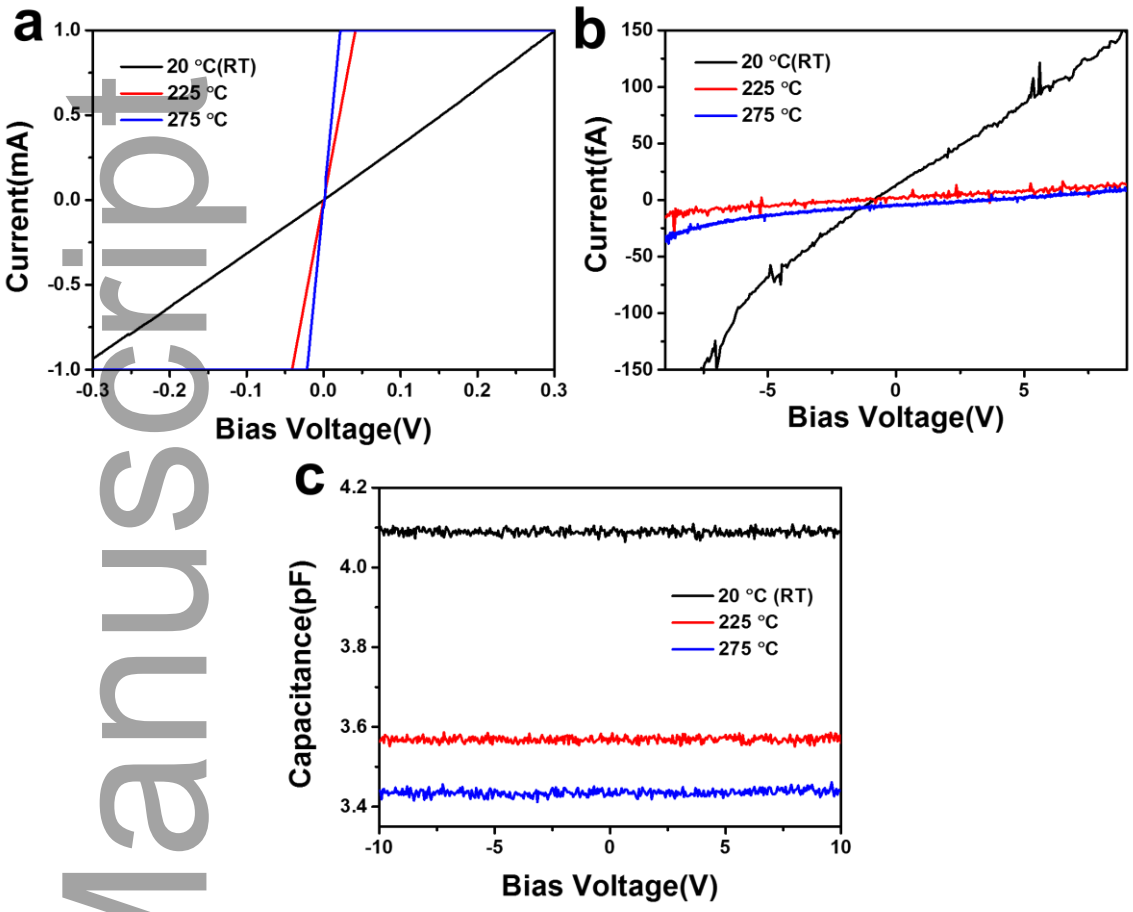

Figure 6. a, Surface IV characteristic measured by probing the top-side surface of the film for room temperature and two annealed samples. b, Bulk IV characteristic measured by probing from the top of the film to the bottom. c, CV measured across the bulk of the non-annealed and two annealed films.

Author Manuscript

This article is protected by copyright. All rights reserved.

EXPERIMENTAL

Chemicals. Tetrachloroaurate (III) trihydrate ($HAuCl_4 \cdot 3H_2O$), sodium citrate tribasic dihydrate ($Na_3C_6H_5O_7 \cdot 2H_2O$), dimethyl sulfoxide (DMSO), and potassium hydroxide (KOH) were all purchased from Sigma-Aldrich and used as received. Bulk Kevlar 69 was purchased from Thread Exchange. E-pure deionized water (18.2 $M\Omega \cdot cm^{-1}$) was obtained from a Millipore Milli-Q system. Glass slides (50 mm × 50 mm, Corning) were cleaned with piranha solution (3:1 v/v H_2SO_4/H_2O_2).

Synthesis of Au NPs. Our synthesis route is straightforward. Typically, gold (III) chloride trihydrate (90.0 mg) was introduced into 475 mL ultrapure deionized water in a glass beaker with appropriate volume equipped with a magnetic stirring bar. The solution was heated to boiling under vigorous stirring followed by additional heating for 20 min. Subsequently, 25 mL of 1.0 wt% sodium citrate solution was added to the gold salt solution. The mixture was heated for 20 min to produce a wine red colored, stable solution, which was cooled to room temperature.

Preparation of ANF films. 10.0 g of bulk Kevlar 69 was dissolved in DMSO with 10.0 g KOH to obtain a 2 wt% ANF solution, which was then magnetically stirred for three weeks at room temperature until a dark red, viscous solution formed.

Spin coating was applied to deposit the ANF films. Glass slides were cleaned with piranha solution, followed by thoroughly rinsing with DI water and compressed air-drying. After setting the glass slide on the disk of the spin coater, 3 mL of ANF solution was dropped and

This article is protected by copyright. All rights reserved.

Author Manuscript

spin-coated at 600 rpm for 30 s. After spin coating, the films were immediately put into DI water to remove the DMSO.

Preparation of Au-ANF films with vacuum filtration (VF). The Au NP solution was forced to penetrate into the ANF films through the vacuum filtration process illustrated in **Supporting Information Figure S4a**. The Au-ANF films with various Au content were prepared under the same conditions and procedures except for the volume of Au NPs solution. Au-ANF films containing 13.9 vol%, 14.7 vol%, 15.7 vol%, 19.6 vol%, 24.8 vol%, 28.9 vol%, 31.6 vol%, and 34.7 vol% of Au consumed 180 mL, 190 mL, 200 mL, 250 mL, 350 mL, 450 mL, 550 mL, and 650 mL of Au NP solution, respectively. The obtained films were subsequently dried in a supercritical CO_2 dryer. The films were dehydrated with ethanol followed by soaking in liquid CO_2 to exchange the pore fluid inside the films with liquid CO_2. Subsequently, the liquid CO_2 was heated to reach the critical point, after which the supercritical CO_2 was slowly decompressed to atmospheric pressure.

Annealing of Au-ANF films. The prepared Au-ANF films were placed in a muffle furnace and annealed at different temperatures (200, 250, 300, 350, and 400 °C) for 20 min.

Characterizations. Transmission electron microscopy (TEM) images were collected by a JEOL 3011 HRTEM. One drop of solution (10 µL) was placed on the surface of a copper grid coated with carbon and dried before testing. The morphologies of ANF films and Au-ANF films were inspected with an FEI Nova Nanolab dual-beam FIB and Scanning Electron Microscope. The distribution of Au NPs in the Au-ANF films were analyzed with an Energy-dispersive X-ray spectroscopy (EDS) mapping conducted in the SEM's EDAX mode

This article is protected by copyright. All rights reserved.

Author Manuscript

(**Supporting Information Figure S10**). The Au-ANF film's Au fractions were determined by a TA Instruments Discovery Thermogravimetric Analyzer (TGA) with a temperature ramp to 700 °C at 10 °C·min^{-1} in a nitrogen at a flow rate of 25 mL·min^{-1}. X-ray diffraction (XRD) patterns of Au NPs, ANF films, and Au-ANF films were collected at ambient temperature using Rigaku Rotating Anode X-Ray Diffractometer with Cu Kα generated at 40 kV and 100 mA. XRD patterns were processed in MDI Jade 5.0 to calculate peak positions, intensity, and full width at half maximum. Fourier transform infrared spectroscopy (FT-IR) was performed on a Nicolet 6700 spectrometer to investigate the chemical properties of Au-ANF films. The samples for FT-IR tests were prepared by spin-coating 1 wt% ANF solutions to obtain ultrathin films with good transmittance. The tensile property of each film was determined using a TA XT Plus Texture Analyzer (Stable Micro Systems Ltd.). The samples were cut into rectangular strips of ~20 mm × 2 mm using a razor blade and five strips were measured for each film. Conductivity measurements with two- and four-probe methods were acquired using a Lucas S-302-4 four points probe station with the Agilent 34401A multimeter. The thickness of Au-ANF films was determined by cross-section SEM images to be ~7.5 µm. A series of five measurements were taken for each film and the data were averaged to give the final reported values. Error bars indicate one standard deviation for the five measurements. The temperature dependence of conductivity measurements was performed from 5 K to 300 K in a Quantum Design Magnetic Property Measurement System (MPMS), equipped with a 5.5 T superconducting magnet, using a Linear Research ac bridge with 16 Hz excitation. The reflectance and transmittance spectra of ANF films and Au-ANF films were measured using the Lambda 900 spectrophotometer equipped with the 150 mm

Author Manuscript

This article is protected by copyright. All rights reserved.

integrating sphere (PerkinElmer). The samples were mounted on the back of the integrating sphere. The angle of incidence light was equal to 8 degrees. The reflected light, which had a large diffuse component, was detected by a photomultiplier tube (PMT) installed in the bottom of the integrating sphere. A standard white diffuse reflector (from Labsphere) was used as a 100 % reference. The IV and CV curves were acquired using a Keithley 4200-SCS semiconductor parameter analyzer and were measured from -10 V to +10 V, in steps of 0.05 V at five different sweep frequencies (100 kHz, 1 MHz, 2 MHz, 5 MHz, and 10 MHz) using a 100 mV_{RMS} drive voltage. The capacitance does not vary for probe frequencies below 1 MHz which was the frequency used to plot the data in **Figure 5c**.

Supporting Information

Supporting Information is available from the Wiley Online Library or from the author.

Acknowledgments:

The central part of this work was supported by the NSF project "Energy- and Cost-Efficient Manufacturing Employing Nanoparticles" NSF 1463474. Partial support of this work was also made by the Center for Photonic and Multiscale Nanomaterials (C-PHOM) funded by the National Science Foundation (NSF) Materials Research Science and Engineering Center program DMR 1120923 as well as NSF projects 1403777; 1411014; 1463474; 1538180. We acknowledge the financial assistance by the China Scholarship Council to J.L, X.W.; and L.L. The authors thank the University of Michigan's EMAL for its assistance with electron microscopy, and for the NSF grant #DMR-9871177 for funding of the JEOL 2010F analytical electron microscope used in this work. The Norfolk State University portion of this work was

This article is protected by copyright. All rights reserved.

Author Manuscript

supported by the NSF PREM grant DMR-1205457, NSF IGERT grant DGE-0966188, HBCU RISE grant NSF HRD-1345215 and ARO grant W911NF-14-1-0639. Additional support was provided by the Basic Research and Applied Research Programs of the US Department of Defense's Defense Threat Reduction Agency (HDTRA-1-11-1-0050, HDTRA1-12-1-0038, HDTRA1-13-C- 0050), as well as the US Department of Homeland Security, Domestic Nuclear Detection Agency (2015-DN-077-097). This support does not constitute an express or implied endorsement on the part of the government.

Author Manuscript

REFERENCES

(1) Li, Y.; Yu, T.; Yang, T.; Zheng, L.; Liao, K. Bio-Inspired Nacre-like Composite Films Based on Graphene with Superior Mechanical, Electrical, and Biocompatible Properties. *Adv. Mater.* **2012**, *24*, 3426–3431.

(2) Cheng, Y.; Lu, S.; Zhang, H.; Varanasi, C. V.; Liu, J. Synergistic Effects from Graphene and Carbon Nanotubes Enable Flexible and Robust Electrodes for High-Performance Supercapacitors. *Nano Lett.* **2012**, *12*, 4206–4211.

(3) Xiao, X.; Li, T.; Yang, P.; Gao, Y.; Jin, H.; Ni, W.; Zhan, W.; Zhang, X.; Cao, Y.; Zhong, J. Fiber-Based All-Solid-State Flexible Supercapacitors for Self-Powered Systems. *ACS Nano* **2012**, *6*, 9200–9206.

This article is protected by copyright. All rights reserved.

(4) Mo, R.; Tung, S. O.; Lei, Z.; Zhao, G.; Sun, K.; Kotov, N. A. Pushing the Limits: 3D Layer-by-Layer-Assembled Composites for Cathodes with 160 C Discharge Rates. *ACS Nano* **2015**, *9*, 5009–5017.

(5) Worsley, M. A.; Kucheyev, S. O.; Kuntz, J. D.; Olson, T. Y.; Han, T. Y.-J.; Hamza, A. V.; Satcher, J. H.; Baumann, T. F. Carbon Scaffolds for Stiff and Highly Conductive Monolithic Oxide–Carbon Nanotube Composites. *Chem. Mater.* **2011**, *23*, 3054–3061.

(6) Coleman, J. N.; Khan, U.; Gun'ko, Y. K. Mechanical Reinforcement of Polymers Using Carbon Nanotubes. *Adv. Mater.* **2006**, *18*, 689–706.

(7) Baughman, R.; Cui, C.; Zakhidov, A.; Iqbal, Z.; Barisci, J.; Spinks, G.; Wallace, G.; Mazzoldi, A.; De Rossi D; Rinzler, A.; *et al.* Carbon Nanotube Actuators. *Science* **1999**, *284*, 1340–1344.

(8) O'Connor, I.; Hayden, H.; Coleman, J. N.; Gun'ko, Y. K. High-Strength, High-Toughness Composite Fibers by Swelling Kevlar in Nanotube Suspensions. *Small* **2009**, *5*, 466–469.

(9) Jan, E.; Hendricks, J. L.; Husaini, V.; Richardson-Burns, S. M.; Sereno, A.; Martin, D. C.; Kotov, N. A. Layered Carbon Nanotube-Polyelectrolyte Electrodes Outperform Traditional Neural Interface Materials. *Nano Lett.* **2009**, *9*, 4012–4018.

Author Manuscript

This article is protected by copyright. All rights reserved.

(10) Zhou, Y.; Han, S.-T.; Xu, Z.-X.; Roy, V. A. L. Low Voltage Flexible Nonvolatile Memory with Gold Nanoparticles Embedded in Poly (methyl Methacrylate). *Nanotechnology* **2012**, *23*, 344014.

(11) Park, S.; Vosguerichian, M.; Bao, Z. A Review of Fabrication and Applications of Carbon Nanotube Film-Based Flexible Electronics. *Nanoscale* **2013**, *5*, 1727–1752.

(12) Sekitani, T.; Zschieschang, U.; Klauk, H.; Someya, T. Flexible Organic Transistors and Circuits with Extreme Bending Stability. *Nat. Mater.* **2010**, *9*, 1015–1022.

(13) Podsiadlo, P.; Kaushik, A. K.; Arruda, E. M.; Waas, A. M.; Shim, B. S.; Xu, J.; Nandivada, H.; Pumplin, B. G.; Lahann, J.; Ramamoorthy, A.; *et al.* Ultrastrong and Stiff Layered Polymer Nanocomposites. *Science* **2007**, *318*, 80–83.

(14) Qian, H.; Bismarck, A.; Greenhalgh, E. S.; Kalinka, G.; Shaffer, M. S. P. Hierarchical Composites Reinforced with Carbon Nanotube Grafted Fibers: The Potential Assessed at the Single Fiber Level. *Chem. Mater.* **2008**, *20*, 1862–1869.

(15) Kildishev, A. V; Boltasseva, A.; Shalaev, V. M. Planar Photonics with Metasurfaces. *Science* **2013**, *339*, 1232009.

(16) Zhang, X.; Li, Q.; Holesinger, T. G.; Arendt, P. N.; Huang, J.; Kirven, P. D.; Clapp, T. G.; DePaula, R. F.; Liao, X.; Zhao, Y.; *et al.* Ultrastrong, Stiff, and Lightweight Carbon-Nanotube Fibers. *Adv. Mater.* **2007**, *19*, 4198–4201.

Author Manuscript

This article is protected by copyright. All rights reserved.

(17) Shim, B. S.; Zhu, J.; Jan, E.; Critchley, K.; Kotov, N. a. Transparent Conductors from Layer-by-Layer Assembled SWNT Films: Importance of Mechanical Properties and a New Figure of Merit. *ACS Nano* **2010**, *4*, 3725–3734.

(18) Kumar, G.; Tang, H. X.; Schroers, J. Nanomoulding with Amorphous Metals. *Nature* **2009**, *457*, 868–872.

(19) Schroers, J.; Lohwongwatana, B.; Johnson, W. L.; Peker, A. Gold Based Bulk Metallic Glass. *Appl. Phys. Lett.* **2005**, *87*, 61912–61913.

(20) Schuster, B. E.; Wei, Q.; Ervin, M. H.; Hruszkewycz, S. O.; Miller, M. K.; Hufnagel, T. C.; Ramesh, K. T. Bulk and Microscale Compressive Properties of a Pd-Based Metallic Glass. *Scr. Mater.* **2007**, *57*, 517–520.

(21) Inoue, A. Stabilization of Metallic Supercooled Liquid. *Acta Mater.* **2000**, *48*, 279–306.

(22) Basu, J.; Ranganathan, S. Bulk Metallic Glasses: A New Class of Engineering Materials. *Sadhana* **2003**, *28*, 783–798.

(23) Johnson, W. L. Bulk Amorphous metal—An Emerging Engineering Material. *Jom* **2002**, *54*, 40–43.

(24) Wang, W.-H.; Dong, C.; Shek, C. H. Bulk Metallic Glasses. *Mater. Sci. Eng. R Reports* **2004**, *44*, 45–89.

Author Manuscript

This article is protected by copyright. All rights reserved.

(25) Inoue, A. Bulk Amorphous and Nanocrystalline Alloys with High Functional Properties. *Mater. Sci. Eng. A* **2001**, *304*, 1–10.

(26) Guo, H.; Yan, P. F.; Wang, Y. B.; Tan, J.; Zhang, Z. F.; Sui, M. L.; Ma, E. Tensile Ductility and Necking of Metallic Glass. *Nat. Mater.* **2007**, *6*, 735–739.

(27) Ashby, M. F.; Greer, A. L. Metallic Glasses as Structural Materials. *Scr. Mater.* **2006**, *54*, 321–326.

(28) Schuh, C. A.; Hufnagel, T. C.; Ramamurty, U. Mechanical Behavior of Amorphous Alloys. *Acta Mater.* **2007**, *55*, 4067–4109.

(29) Hasegawa, R. Applications of Amorphous Magnetic Alloys. *Mater. Sci. Eng. A* **2004**, *375*, 90–97.

(30) Kumar, G.; Desai, A.; Schroers, J. Bulk Metallic Glass: The Smaller the Better. *Adv. Mater.* **2011**, *23*, 461–476.

(31) Chen, M. Mechanical Behavior of Metallic Glasses: Microscopic Understanding of Strength and Ductility. *Annu. Rev. Mater. Res.* **2008**, *38*, 445–469.

(32) Yamasaki, M.; Kagao, S.; Kawamura, Y.; Yoshimura, K. Thermal Diffusivity and Conductivity of Supercooled Liquid in $Zr_{41}Ti_{14}Cu_{12}Ni_{10}Be_{23}$ Metallic Glass. *Appl. Phys. Lett.* **2004**, *84*, 4653.

Author Manuscript

This article is protected by copyright. All rights reserved.

(33) Yamauchi, R.; Hata, S.; Sakurai, J.; Shimokohbe, A. Combinatorial Search for Low Resistivity Pd-Cu-Si Thin Film Metallic Glass Compositions. *Japanese J. Appl. Physics, Part 1 Regul. Pap. Short Notes Rev. Pap.* **2006**, *45*, 5911–5919.

(34) Sanchez, C.; Julian, B.; Belleville, P.; Popall, M. Applications of Hybrid Organic–inorganic Nanocomposites. *J. Mater. Chem.* **2005**, *15*, 3559–3592.

(35) Mamedov, A. a; Kotov, N. a; Prato, M.; Guldi, D. M.; Wicksted, J. P.; Hirsch, A. Molecular Design of Strong Single-Wall Carbon Nanotube/polyelectrolyte Multilayer Composites. *Nat. Mater.* **2002**, *1*, 190–194.

(36) Jancar, J.; Douglas, J. F.; Starr, F. W.; Kumar, S. K.; Cassagnau, P.; Lesser, a. J.; Sternstein, S. S.; Buehler, M. J. Current Issues in Research on Structure-Property Relationships in Polymer Nanocomposites. *Polymer* **2010**, *51*, 3321–3343.

(37) Yetisen, A. K.; Qu, H.; Manbachi, A.; Butt, H.; Dokmeci, M. R.; Hinestroza, J. P.; Skorobogatiy, M.; Khademhosseini, A.; Yun, S. H. Nanotechnology in Textiles. *ACS Nano* **2016**, *10*, 3042–3068.

(38) Kaltenbrunner, M.; Sekitani, T.; Reeder, J.; Yokota, T.; Kuribara, K.; Tokuhara, T.; Drack, M.; Schwödiauer, R.; Graz, I.; Bauer-Gogonea, S.; *et al.* An Ultra-Lightweight Design for Imperceptible Plastic Electronics. *Nature* **2013**, *499*, 458–463.

(39) Kim, D.-H.; Lu, N.; Ma, R.; Kim, Y.-S.; Kim, R.-H.; Wang, S.; Wu, J.; Won, S. M.; Tao, H.; Islam, A.; *et al.* Epidermal Electronics. *Science* **2011**, *333*, 838–843.

Author Manuscript

This article is protected by copyright. All rights reserved.

(40) Schwartz, G.; Tee, B. C.-K.; Mei, J.; Appleton, A. L.; Kim, D. H.; Wang, H.; Bao, Z. Flexible Polymer Transistors with High Pressure Sensitivity for Application in Electronic Skin and Health Monitoring. *Nat. Commun.* **2013**, *4*, 1859.

(41) Shim, B. S.; Chen, W.; Doty, C.; Xu, C.; Kotov, N. A. Smart Electronic Yarns and Wearable Fabrics for Human Biomonitoring Made by Carbon Nanotube Coating with Polyelectrolytes. *Nano Lett.* **2008**, *8*, 4151–4157.

(42) Zhang, J.; Landry, M. P.; Barone, P. W.; Kim, J.-H.; Lin, S.; Ulissi, Z. W.; Lin, D.; Mu, B.; Boghossian, A. A.; Hilmer, A. J.; *et al.* Molecular Recognition Using Corona Phase Complexes Made of Synthetic Polymers Adsorbed on Carbon Nanotubes. *Nat. Nanotechnol.* **2013**, *8*, 959–968.

(43) Tung, S.-O.; Ho, S.; Yang, M.; Zhang, R.; Kotov, N. A. A Dendrite-Suppressing Composite Ion Conductor from Aramid Nanofibres. *Nat. Commun.* **2015**, *6*, 6152.

(44) Vu, A.; Stein, A. Multiconstituent Synthesis of $LiFePO_4$/C Composites with Hierarchical Porosity as Cathode Materials for Lithium Ion Batteries. *Chem. Mater.* **2011**, *23*, 3237–3245.

(45) Huang, H.; Yin, S.-C.; Kerr, T.; Taylor, N.; Nazar, L. F. Nanostructured Composites: A High Capacity, Fast Rate $Li_3V_2(PO_4)_3$/Carbon Cathode for Rechargeable Lithium Batteries. *Adv. Mater.* **2002**, *14*, 1525–1528.

Author Manuscript

This article is protected by copyright. All rights reserved.

(46) Liu, Y.; Zhu, M.; Chen, D. Sheet-like $MoSe_2$/C Composites with Enhanced Li-Ion Storage Properties. *J. Mater. Chem. A* **2015**, *3*, 11857–11862.

(47) Chang, K.; Chen, W. L-Cysteine-Assisted Synthesis of Layered MoS_2/graphene Composites with Excellent Electrochemical Performances for Lithium Ion Batteries. *ACS Nano* **2011**, *5*, 4720–4728.

(48) Zhang, H.; Patel, P. R.; Xie, Z.; Swanson, S. D.; Wang, X.; Kotov, N. A. Tissue-Compliant Neural Implants from Microfabricated Carbon Nanotube Multilayer Composite. *ACS Nano* **2013**, *7*, 7619–7629.

(49) Zhang, H.; Shih, J.; Zhu, J.; Kotov, N. A. Layered Nanocomposites from Gold Nanoparticles for Neural Prosthetic Devices. *Nano Lett.* **2012**, *12*, 3391–3398.

(50) Kim, D.-H.; Viventi, J.; Amsden, J. J.; Xiao, J.; Vigeland, L.; Kim, Y.-S.; Blanco, J. A.; Panilaitis, B.; Frechette, E. S.; Contreras, D.; *et al.* Dissolvable Films of Silk Fibroin for Ultrathin Conformal Bio-Integrated Electronics. *Nat. Mater.* **2010**, *9*, 511–517.

(51) Reuter, T.; Vidoni, O.; Torma, V.; Schmid, G.; Nan, L.; Gleiche, M.; Chi, L.; Fuchs, H. Two-Dimensional Networks via Quasi One-Dimensional Arrangements of Gold Clusters. *Nano Lett.* **2002**, *2*, 709–711.

(52) Choudhary, A.; Singh, G.; Biradar, A. M. Advances in Gold Nanoparticle-Liquid Crystal Composites. *Nanoscale* **2014**, *6*, 7743–7756.

Author Manuscript

This article is protected by copyright. All rights reserved.

(53) Ryu, D.; Loh, K. J.; Ireland, R.; Karimzada, M.; Yaghmaie, F.; Gusman, A. M. In Situ Reduction of Gold Nanoparticles in PDMS Matrices and Applications for Large Strain Sensing. *Smart Struct. Syst.* **2011**, *8*, 471–486.

(54) Ismaili, H.; Geng, D.; Sun, A. X.; Kantzas, T. T.; Workentin, M. S. Light-Activated Covalent Formation of Gold Nanoparticle-Graphene and Gold Nanoparticle-Glass Composites. *Langmuir* **2011**, *27*, 13261–13268.

(55) Kim, B.; Sigmund, W. M. Functionalized Multiwall Carbon Nanotube/gold Nanoparticle Composites. *Langmuir* **2004**, *20*, 8239–8242.

(56) Cai, J.; Kimura, S.; Wada, M.; Kuga, S. Nanoporous Cellulose as Metal Nanoparticles Support. *Biomacromolecules* **2009**, *10*, 87–94.

(57) Schlicke, H.; Schröder, J. H.; Trebbin, M.; Petrov, A.; Ijeh, M.; Weller, H.; Vossmeyer, T. Freestanding Films of Crosslinked Gold Nanoparticles Prepared via Layer-by-Layer Spin-Coating. *Nanotechnology* **2011**, *22*, 305303.

(58) Jiang, C.; Markutsya, S.; Pikus, Y.; Tsukruk, V. V. Freely Suspended Nanocomposite Membranes as Highly Sensitive Sensors. *Nat. Mater.* **2004**, *3*, 721–728.

(59) Yonezawa, T.; Matsune, H.; Kunitake, T. Layered Nanocomposite of Close-Packed Gold Nanoparticles and TiO_2 Gel Layers. *Chem. Mater.* **1999**, *11*, 33–35.

Author Manuscript

This article is protected by copyright. All rights reserved.

(60) Ariga, K.; Yamauchi, Y.; Rydzek, G.; Ji, Q.; Yonamine, Y.; Wu, K. C.-W.; Hill, J. P. Layer-by-Layer Nanoarchitectonics: Invention, Innovation, and Evolution. *Chem. Lett.* **2014**, *43*, 36–68.

(61) Kim, Y.; Zhu, J.; Yeom, B.; Di Prima, M.; Su, X.; Kim, J.-G.; Yoo, S. J.; Uher, C.; Kotov, N. A. Stretchable Nanoparticle Conductors with Self-Organized Conductive Pathways. *Nature* **2013**, *500*, 59–63.

(62) Shyu, T. C.; Damasceno, P. F.; Dodd, P. M.; Lamoureux, A.; Xu, L.; Shlian, M.; Shtein, M.; Glotzer, S. C.; Kotov, N. A. A Kirigami Approach to Engineering Elasticity in Nanocomposites through Patterned Defects. *Nat. Mater.* **2015**, *14*, 785–789.

(63) Yang, M.; Cao, K.; Sui, L.; Qi, Y.; Zhu, J.; Waas, A.; Arruda, E. M.; Kieffer, J.; Thouless, M. D.; Kotov, N. A. Dispersions of Aramid Nanofibers: A New Nanoscale Building Block. *ACS Nano* **2011**, *5*, 6945–6954.

(64) Iijima, M.; Kamiya, H. Non-Aqueous Colloidal Processing Route for Fabrication of Highly Dispersed Aramid Nanofibers Attached with Ag Nanoparticles and Their Stability in Epoxy Matrixes. *Colloids Surfaces A Physicochem. Eng. Asp.* **2015**, *482*, 195–202.

(65) Zhu, J.; Cao, W.; Yue, M.; Hou, Y.; Han, J.; Yang, M. Strong and Stiff Aramid Nanofiber/ Carbon Nanotube Nanocomposites. *ACS Nano* **2015**, *9*, 2489–2501.

Author Manuscript

This article is protected by copyright. All rights reserved.

(66) Fan, J.; Shi, Z.; Tian, M.; Yin, J. Graphene–aramid Nanofiber Nanocomposite Paper with High Mechanical and Electrical Performance. *RSC Adv.* **2013**, *3*, 17664 -17667.

(67) Kuang, Q.; Zhang, D.; Yu, J. C.; Chang, Y. W.; Yue, M.; Hou, Y.; Yang, M. Toward Record-High Stiffness in Polyurethane Nanocomposites Using Aramid Nanofibers. *J. Phys. Chem. C* **2015**, *119*, 27467–27477.

(68) Ariga, K.; Vinu, A.; Yamauchi, Y.; Ji, Q.; Hill, J. P. Nanoarchitectonics for Mesoporous Materials. *Bull. Chem. Soc. Jpn.* **2012**, *85*, 1–32.

(69) Decher, G.; Schlenoff, J. B. Multilayer Thin Films: Sequential Assembly of Nanocomposite Materials; Wiley-VCH, Weinheim, Germany **2006**.

(70) Xi, Q.; Chen, X.; Evans, D. G.; Yang, W. Gold Nanoparticle-Embedded Porous Graphene Thin Films Fabricated via Layer-by-Layer Self-Assembly and Subsequent Thermal Annealing for Electrochemical Sensing. *Langmuir* **2012**, *28*, 9885–9892.

(71) Wang, J.; Yao, H.-B.; He, D.; Zhang, C.-L.; Yu, S.-H. Facile Fabrication of Gold Nanoparticles-Poly (vinyl Alcohol) Electrospun Water-Stable Nanofibrous Mats: Efficient Substrate Materials for Biosensors. *ACS Appl. Mater. Interfaces* **2012**, *4*, 1963–1971.

(72) Huang, J.; Kunitake, T.; Onoue, S.-Y. A Facile Route to a Highly Stabilized Hierarchical Hybrid of Titania Nanotube and Gold Nanoparticle. *Chem. Commun.* **2004**, 1008–1009.

Author Manuscript

This article is protected by copyright. All rights reserved.

(73) Qiu, L.; Liu, J. Z.; Chang, S. L. Y.; Wu, Y.; Li, D. Biomimetic Superelastic Graphene-Based Cellular Monoliths. *Nat. Commun.* **2012**, *3*, 1241.

(74) Han, S.; Wu, D.; Li, S.; Zhang, F.; Feng, X. Porous Graphene Materials for Advanced Electrochemical Energy Storage and Conversion Devices. *Adv. Mater.* **2014**, *26*, 849–864.

(75) Jayaprakash, N.; Shen, J.; Moganty, S. S.; Corona, A.; Archer, L. A. Porous Hollow Carbon@Sulfur Composites for High-Power Lithium-Sulfur Batteries. *Angew. Chemie* **2011**, *123*, 6026–6030.

(76) Jiang, L.; Fan, Z. Design of Advanced Porous Graphene Materials: From Graphene Nanomesh to 3D Architectures. *Nanoscale* **2014**, *6*, 1922–1945.

(77) Lvov, Y.; Yamada, S.; Kunitake, T. Non-Linear Optical Effects in Layer-by-Layer Alternate Films of Polycations and an Azobenzene-Containing Polyanion. *Thin Solid Films* **1997**, *300*, 107–112.

(78) Ariga, K.; Ji, Q.; Hill, J. P.; Bando, Y.; Aono, M. Forming Nanomaterials as Layered Functional Structures toward Materials Nanoarchitectonics. *NPG Asia Mater.* **2012**, *4*, e17.

(79) Park, J. I.; Nguyen, T. D.; de Queirós Silveira, G.; Bahng, J. H.; Srivastava, S.; Zhao, G.; Sun, K.; Zhang, P.; Glotzer, S. C.; Kotov, N. A. Terminal Supraparticle Assemblies from Similarly Charged Protein Molecules and Nanoparticles. *Nat. Commun.* **2014**, *5*, 3593

Author Manuscript

This article is protected by copyright. All rights reserved.

(80) Xia, Y.; Nguyen, T. D.; Yang, M.; Lee, B.; Santos, A.; Podsiadlo, P.; Tang, Z.; Glotzer, S. C.; Kotov, N. A. Self-Assembly of Self-Limiting Monodisperse Supraparticles from Polydisperse Nanoparticles. *Nat. Nanotechnol.* **2011**, *6*, 580–587.

(81) Piccinini, E.; Pallarola, D.; Battaglini, F.; Azzaroni, O. Self-Limited Self-Assembly of Nanoparticles into Supraparticles: Towards Supramolecular Colloidal Materials by Design. *Mol. Syst. Des. Eng.* **2016**, *1*, 155–162.

(82) Feng, H.; Yang, Y.; You, Y.; Li, G.; Guo, J.; Yu, T.; Shen, Z.; Wu, T.; Xing, B. Simple and Rapid Synthesis of Ultrathin Gold Nanowires, Their Self-Assembly and Application in Surface-Enhanced Raman Scattering. *Chem. Commun.* **2009**, 1984–1986.

(83) Kwon, Y. N.; Leckie, J. O. Hypochlorite Degradation of Crosslinked Polyamide Membranes. II. Changes in Hydrogen Bonding Behavior and Performance. *J. Memb. Sci.* **2006**, *282*, 456–464.

(84) Jiang, H.; Moon, K.; Li, Y.; Wong, C. P. Surface Functionalized Silver Nanoparticles for Ultrahigh Conductive Polymer Composites. *Chem. Mater.* **2006**, *18*, 2969–2973.

(85) Im, J.; Singh, J.; Soares, J. W.; Steeves, D. M.; Whitten, J. E. Synthesis and Optical Properties of Dithiol-Linked ZnO/Gold Nanoparticle Composites. *J. Phys. Chem. C* **2011**, *115*, 10518–10523.

Author Manuscript

This article is protected by copyright. All rights reserved.

(86) Schlesinger, M.; Giese, M.; Blusch, L. K.; Hamad, W. Y.; MacLachlan, M. J. Chiral Nematic Cellulose-Gold Nanoparticle Composites from Mesoporous Photonic Cellulose. *Chem. Commun.* **2015**, *51*, 530–533.

(87) Acreman, A.; Kaczmarek, M.; D'Alessandro, G. Gold Nanoparticle Liquid Crystal Composites as a Tunable Nonlinear Medium. *Phys. Rev. E* **2014**, *90*, 012504.

(88) Psarras, G. C. Hopping Conductivity in Polymer Matrix-Metal Particles Composites. *Compos. Part A Appl. Sci. Manuf.* **2006**, *37*, 1545–1553.

(89) Powell, M. Site Percolation in Randomly Packed Spheres. *Phys. Rev. B* **1979**, *20*, 4194–4198.

(90) Fu, S.-Y.; Feng, X.-Q.; Lauke, B.; Mai, Y.-W. Effects of Particle Size, Particle/matrix Interface Adhesion and Particle Loading on Mechanical Properties of Particulate–polymer Composites. *Compos. Part B Eng.* **2008**, *39*, 933–961.

(91) He, L.; Tjong, S. C. Facile Synthesis of Silver-Decorated Reduced Graphene Oxide as a Hybrid Filler Material for Electrically Conductive Polymer Composites. *RSC Adv.* **2015**, *5*, 15070–15076.

(92) Liang, G. D.; Bao, S. P.; Tjong, S. C. Microstructure and Properties of Polypropylene Composites Filled with Silver and Carbon Nanotube Nanoparticles Prepared by Melt-Compounding. *Mater. Sci. Eng. B* **2007**, *142*, 55–61.

Author Manuscript

This article is protected by copyright. All rights reserved.

(93) Lee, J.; Lee, P.; Lee, H.; Lee, D.; Lee, S. S.; Ko, S. H. Very Long Ag Nanowire Synthesis and Its Application in a Highly Transparent, Conductive and Flexible Metal Electrode Touch Panel. *Nanoscale* **2012**, *4*, 6408-6414.

(94) Huang, L.-J.; Ren, N.-F.; Li, B.-J.; Zhou, M. Effect of Annealing on the Morphology, Structure and Photoelectric Properties of AZO/Pt/FTO Trilayer Films. *Acta Metall. Sin.* **2015**, *28*, 281–288.

(95) Chun, K.-Y.; Oh, Y.; Rho, J.; Ahn, J.-H.; Kim, Y.-J.; Choi, H. R.; Baik, S. Highly Conductive, Printable and Stretchable Composite Films of Carbon Nanotubes and Silver. *Nat. Nanotechnol.* **2010**, *5*, 853–857.

(96) Greer, J. R.; Street, R. A. Thermal Cure Effects on Electrical Performance of Nanoparticle Silver Inks. *Acta Mater.* **2007**, *55*, 6345–6349.

(97) Vadukumpully, S.; Paul, J.; Mahanta, N.; Valiyaveettil, S. Flexible Conductive Graphene/poly(vinyl Chloride) Composite Thin Films with High Mechanical Strength and Thermal Stability. *Carbon* **2011**, *49*, 198–205.

(98) Song, P.; Cao, Z.; Cai, Y.; Zhao, L.; Fang, Z.; Fu, S. Fabrication of Exfoliated Graphene-Based Polypropylene Nanocomposites with Enhanced Mechanical and Thermal Properties. *Polymer* **2011**, *52*, 4001–4010.

(99) Luong, N. D.; Hippi, U.; Korhonen, J. T.; Soininen, A. J.; Ruokolainen, J.; Johansson, L. S.; Nam, J. Do; Sinh, L. H.; Seppälä, J. Enhanced Mechanical and Electrical Properties

Author Manuscript

This article is protected by copyright. All rights reserved.

of Polyimide Film by Graphene Sheets via in Situ Polymerization. *Polymer* **2011**, *52*, 5237–5242.

(100) He, L.; Tjong, S. C. Facile Synthesis of Silver-Decorated Reduced Graphene Oxide as a Hybrid Filler Material for Electrically Conductive Polymer Composites. *RSC Adv.* **2015**, *5*, 15070–15076.

(101) Luong, N. D.; Pahimanolis, N.; Hippi, U.; Korhonen, J. T.; Ruokolainen, J.; Johansson, L.-S.; Nam, J.-D.; Seppala, J. Graphene/cellulose Nanocomposite Paper with High Electrical and Mechanical Performances. *J. Mater. Chem.* **2011**, *21*, 13991–13998.

(102) Wang, X.; Bai, H.; Yao, Z.; Liu, A.; Shi, G. Electrically Conductive and Mechanically Strong Biomimetic Chitosan/reduced Graphene Oxide Composite Films. *J. Mater. Chem.* **2010**, *20*, 9032-9036.

(103) Chen, J.; Ramasubramaniam, R.; Xue, C.; Liu, H. A Versatile, Molecular Engineering Approach to Simultaneously Enhanced, Multifunctional Carbon Nanotube-Polymer Composites. *Adv. Funct. Mater.* **2006**, *16*, 114–119.

(104) Gorrasi, G.; Sarno, M.; Bartolomeo, A. Di; Sannino, D.; Ciambelli, P.; Vittoria, V. Incorporation of Carbon Nanotubes into Polyethylene by High Energy Ball Milling: Morphology and Physical Properties. *J. Polym. Sci. Part B Polym. Phys.* **2007**, *45*, 597–606.

Author Manuscript

This article is protected by copyright. All rights reserved.

(105) Allaoui, A.; Bai, S.; Cheng, H. M.; Bai, J. B. Mechanical and Electrical Properties of a MWNT/epoxy Composite. *Compos. Sci. Technol.* **2002**, *62*, 1993–1998.

(106) McNally, T.; Potschke, P.; Halley, P.; Murphy, M.; Martin, D.; Bell, S. E. J.; Brennan, G. P.; Bein, D.; Lemoine, P.; Quinn, J. P. Polyethylene Multiwalled Carbon Nanotube Composites. *Polymer* **2005**, *46*, 8222–8232.

(107) Choi, Y.-K.; Sugimoto, K.; Song, S.-M.; Gotoh, Y.; Ohkoshi, Y.; Endo, M. Mechanical and Physical Properties of Epoxy Composites Reinforced by Vapor Grown Carbon Nanofibers. *Carbon* **2005**, *43*, 2199–2208.

(108) Yuen, S. M.; Ma, C. C. M.; Lin, Y. Y.; Kuan, H. C. Preparation, Morphology and Properties of Acid and Amine Modified Multiwalled Carbon Nanotube/polyimide Composite. *Compos. Sci. Technol.* **2007**, *67*, 2564–2573.

(109) Hu, W.; Chen, S.; Yang, Z.; Liu, L.; Wang, H. Flexible Electrically Conductive Nanocomposite Membrane Based on Bacterial Cellulose and Polyaniline. *J. Phys. Chem. B* **2011**, *115*, 8453–8457.

(110) Zhang, B.; Zhao, D. Q.; Pan, M. X.; Wang, W. H.; Greer, A. L. Amorphous Metallic Plastic. *Phys. Rev. Lett.* **2005**, *94*, 1–4.

(111) Inoue, A.; Zhang, T.; Kita, K.; Masumoto, T. Mechanical Strength, Thermal Stability and Electrical Resistivity of Aluminium-Rare Earth Metal Binary Amorphous Alloys, 1989, 870–877.

Author Manuscript

This article is protected by copyright. All rights reserved.

(112) Liu, Y.; Hata, S.; Wada, K.; Shimokohbe, A. Thermal, Mechanical and Electrical Properties of Pd-Based Thin-Film Metallic Glass. *Jpn. J. Appl. Phys.* **2001**, *40*, 5382–5388.

A composite based on aramid nanofibers (ANFs) and gold nanoparticles (NP) reveals high mechanical properties and conductivity being competitive or better with best nanocomposites and even amorphous metals. Gold nanoparticles are self-assembled in chains on ANFs, which reduces percolation threshold. High temperature stability of ANF makes possible annealing of NPs that further facilitates charge transport. The scalable fabrication of the free-standing porous composites sheets leads to ground-breaking materials for wearable electronics and plasmonics.

Author Manuscript

This article is protected by copyright. All rights reserved.